




## Electrical circuit realization of topological switching for the non-Hermitian skin effect

Hanxu Zhang <sup>1,\*</sup>, Tian Chen <sup>1,\*†</sup>, Linhu Li,<sup>2</sup> Ching Hua Lee,<sup>3</sup> and Xiangdong Zhang <sup>1,‡</sup>

<sup>1</sup>Key Laboratory of Advanced Optoelectronic Quantum Architecture and Measurements of Ministry of Education, Beijing Key Laboratory of Nanophotonics & Ultrafine Optoelectronic Systems, School of Physics, Beijing Institute of Technology, Beijing 100081, China

<sup>2</sup>Guangdong Provincial Key Laboratory of Quantum Metrology and Sensing and School of Physics and Astronomy, Sun Yat-Sen University (Zhuhai Campus), Zhuhai 519082, China

<sup>3</sup>Department of Physics, National University of Singapore, Singapore 117542



(Received 30 September 2022; revised 31 January 2023; accepted 15 February 2023; published 24 February 2023)

Non-Hermitian systems reveal rich physics beyond the Hermitian regime, and have aroused great interest. One remarkable physical phenomenon is the non-Hermitian skin effect. Recently, topological switching for the non-Hermitian skin effect has been theoretically proposed in cold-atom systems. However, experimental realization of such a phenomenon remains a great challenge. Here, we theoretically propose and experimentally demonstrate a topological switch for the non-Hermitian skin effect in electrical circuit networks. By controlling the operational amplifier and other electric components, the nonreciprocal transport of probability for electrical signals is observed when the switch is turned on. Furthermore, the robustness of such a topological switch is demonstrated both theoretically and experimentally when perturbations are added. Our study provides an avenue for controlling electrical signals in circuit networks, with potential applications in the field of integrated circuit design.

DOI: [10.1103/PhysRevB.107.085426](https://doi.org/10.1103/PhysRevB.107.085426)

### I. INTRODUCTION

In recent years, there has been a great deal of interest in studying non-Hermitian systems due to the exhibition of properties that are different from those in Hermitian systems [1–35]. The non-Hermitian skin effect (NHSE), namely, that the majority of eigenstates of a non-Hermitian operator are localized at boundaries, is one of the most remarkable phenomena in non-Hermitian systems [36–50]. The interplay of the NHSE with topology is particularly interesting [51], and has been observed in experiments [52,53]. If such a phenomenon can be finely controlled, there should be many potential applications. Recently, a topological switch for the non-Hermitian skin effect has been theoretically proposed in cold-atom systems [54]. This switch is controlled by atom loss. When the non-Hermitian skin effect is switched on, wave packets are transported with nonreciprocal amplification. Unfortunately, the precise control of atom loss is difficult, thus making the experimental observation of topological switching almost impossible in cold-atom experiments.

On the other hand, electric circuits have been widely used to simulate quantum phenomena and topological states [41,45,46,52,55–66]. Non-Hermitian Laplacians can be realized in the circuit by introducing operational amplifiers (op-amps), analog multipliers, resistor, and other electrical circuit components [41,45,46,52,58–62]. Based on such realization, the skin effect in the non-Hermitian circuit lattice has

been experimentally demonstrated [41,49,52]. With appropriate arrangement of op-amps in higher spatial dimensions, the hybrid topological-skin effect has also been observed [52]. In these experimental observations, the circuit Laplacians corresponding to the non-Hermitian Hamiltonians are constructed, and the non-Hermitian skin effect can be demonstrated by measuring the impedance of a circuit at steady state. One thus wonders if topological switching of the non-Hermitian skin effect can also be realized in designed circuit networks.

In this work, we propose theoretically and demonstrate experimentally that the topological switch for the non-Hermitian skin effect can be realized in circuit networks. The circuit networks are designed to simulate dynamics evolution behavior in the quantum system based on the similarity between circuit Laplacians and lattice Hamiltonians. The dynamical evolution behavior is observed and the topological switch for the non-Hermitian skin effect is demonstrated experimentally.

### II. THEORETICAL CIRCUIT DESIGN TO REALIZE THE TOPOLOGICAL SWITCH

In Fig. 1(a), we provide a circuit where the nodes in black connect to each other by op-amp structure with various colors. The lattice corresponding to this circuit is shown in Fig. 1(b). In Fig. 1(b),  $c_v e^{-i\varphi}$  is the coupling between different sublattices of the cell,  $c_{\uparrow,y}$ ,  $c_{\downarrow,y}$ ,  $c'_{\uparrow,y}$ ,  $c'_{\downarrow,y}$ ,  $c_{\uparrow,x}$ , and  $c_{\downarrow,x}$  are the couplings between the same sublattices in the different cells, and  $c_{d,x}$  is the coupling between different sublattices of the different cells. In addition,  $c_{\Delta-}$  represents an energy offset between the sublattices, and  $ic_g$  is the loss. To display the evolution of the lattice, the nodes of the circuit in Fig. 1(a) are twice as many as the nodes in the lattice in Fig. 1(b), and

\*These authors contributed equally to this work.

†chentian@bit.edu.cn

‡zhangxd@bit.edu.cn

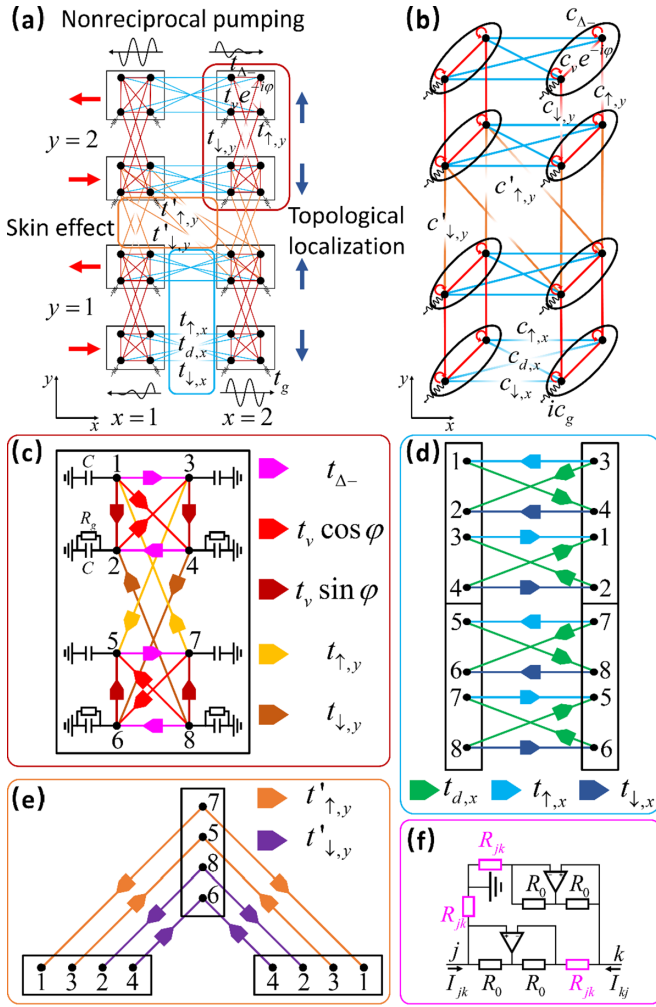


FIG. 1. Theoretical design of the circuit network. (a) The circuit structure with four unit cells. Nodes in black connect to each other by op-amp structure (simplified to colored lines). With the  $x$ - $y$  coordinate axis, we can identify a unit cell by  $(x, y)$ . For example, the unit cell in  $(2, 2)$  is the unit cell in the upper-right corner marked by a red box. (b) The lattice corresponding to the circuit. The black ellipse, corresponding to the black box in (a), is the unit cell in the lattice, and it contains two black sublattices. The different symbols “ $c$ ” indicate the couplings between different sublattices. (c) The unit cell (the red part) in the circuit containing eight nodes, which are labeled 1–8. For clarity, this part of the connection is colored red in Fig. 1(a) and is different colors in Fig. 1(c). All nodes are grounded by a capacitor with value  $C$ , and the resistance  $R_g$  is added to the nodes with the even number. The connections between these nodes are op-amp structure, with different parameters that are marked by different colors. The nodes 1 and 3 correspond to the real and imaginary parts of the upper lattices, nodes 2 and 4 correspond to another sublattice, and so do nodes 5–8. (d), (e) The connection between different unit cells along the  $x$  direction (blue part) and the  $y$  direction (orange part), respectively. For clarity, these parts of connections are colored blue or orange in (a) and more detailed colors in (c), (d). (f) Details of the op-amp structure. The op-amp structure is used to control the current, so that  $I_{jk} = V_k/R_{jk}$  and  $I_{kj} = -V_j/R_{jk}$ , which is used for the correspondence between the circuit matrix and the quantum Hamiltonian. The value of resistance  $R_0$  is the same for all op-amps, and the value of resistance  $R_{jk}$  is inversely related to the “coupling” strength between two sublattices in the circuit.

the connections in the circuit with the symbol “ $t$ ” are twice as many as the couplings in the lattice with the symbol “ $c$ .”

The circuit in Fig. 1(a) can be divided into three parts, the circuit unit cell as shown in Fig. 1(c) in red, the  $x$ -direction connection as shown in Fig. 1(d) in blue, and the  $y$ -direction connection as shown in Fig. 1(e) in orange. In the circuit unit cell, each sublattice is connected to the ground by an electric capacitance  $C$  whose value is the same for all sublattices. A resistance  $R_g = 1/(2t_g)$ , which represents the “loss” in the circuit system, is used to connect the ground and the sublattice with an even value  $j$ . In addition, the nodes in the circuit connect to each other with the op-amp structure shown in Fig. 1(f). The op-amp structure has two kinds of resistance, one with constant value  $R_0$  and another with variable value  $R_{jk}$ , which is inversely proportional to the coupling strength in the circuit. Taking the rose-color op-amp structure ( $t_{\Delta-}$ ) as an example, the value of  $R_{jk}$  satisfies  $CR_{jk} = 1/|t_{\Delta-}|$ . The op-amp structure adjusts the current to  $I_{jk} = V_k/R_{jk}$  and  $I_{kj} = -V_j/R_{jk}$ , which is used for the correspondence between the circuit matrix and the quantum Hamiltonian in the following text. For clarity, we take  $R'_{jk} = R_{jk}$  and  $R'_{kj} = -R_{jk}$ . Details have been shown in Appendix A.

As discussed in Refs. [52,54], the lattice in Fig. 1(b) can possess the non-Hermitian skin effect in the  $x$  direction by the loss, and induce the topology in the  $y$  direction, which results in a typical skin-topological effect controlled by the topology. It also has the ability to switch on and off the skin effect through controlling the reciprocity along the  $x$  direction [54]. Here, based on the circuit networks in Fig. 1(a), we can realize the topological switch for the non-Hermitian skin effect. When the switch is off, the nonreciprocity with two sublattices favoring opposite directions can be balanced by intersubattice couplings and yields net reciprocity. When the switch is on, the reciprocity is broken when topological boundary modes localize on the edge, such that nonreciprocal pumping dominates.

Moreover, due to the extensibility of the circuit, it is convenient to study the three-dimensional model. We can stack the two-dimensional circuit and apply the connection to the  $z$  direction. For example, we can connect the nodes in the  $z$  direction similar to the case in the  $x$  direction as shown in Fig. 1(d), so the similar non-Hermitian skin effect appears. This three-dimensional circuit is the skin-topological-skin model. More various controlling results can be found in this three-dimensional circuit.

Suppose that the circuit in Fig. 1(a) has  $2N$  nodes, and  $V_j(t)$  represents the voltage at the  $j$ th node. According to the circuit design above, the Kirchhoff equation for  $V_j(t)$  is expressed as

$$C \frac{dV_j}{dt} + \frac{V_j}{R_g} + \sum_{j \neq k} I_{jk} = C \frac{dV_j}{dt} + \frac{V_j}{R_g} + \sum_{j \neq k} \frac{V_k}{R'_{jk}} = 0. \quad (1)$$

We can use a column vector  $|V(t)\rangle = [V_1(t), V_2(t), \dots, V_{2N}(t)]^T$  to express the voltages at the  $2N$  nodes at time  $t$ , and the superscript “ $T$ ” denotes the transpose operation. So the dynamics of the voltages for these  $2N$  nodes is

$$\frac{d|V(t)\rangle}{dt} = A|V(t)\rangle \Rightarrow i \frac{d|V(t)\rangle}{dt} = iA|V(t)\rangle. \quad (2)$$

The circuit Laplacian matrix  $A$  governs the dynamics of the voltages. The element of the matrix is expressed as  $A_{jk} = \frac{1}{CR'_{jk}} = -A_{kj}$ . Based on the description above, the value of  $R'_{jk}$  is inversely related to the ‘‘coupling’’ strength

$$A(k_x, k_y) = \begin{bmatrix} g(\sigma_3 - \sigma_0)\tau_0 - it_v \sin \varphi \sigma_2 \tau_3 & -[\sigma_0 a_\sigma^+ + \sigma_3 a_\sigma^- + a_\tau^+ \tau_0 + a_\tau^- \tau_3] \\ \sigma_0 a_\sigma^+ + \sigma_3 a_\sigma^- + a_\tau^+ \tau_0 + a_\tau^- \tau_3 & g(\sigma_3 - \sigma_0)\tau_0 - it_v \sin \varphi \sigma_2 \tau_3 \end{bmatrix}, \quad (3)$$

where  $a_\sigma^\pm = -(2t_{\pm,x} \cos k_x - \Delta_\pm)\tau_0 - \{t_{\pm,y} + t'_{\pm,y}[\cos k_y + \cos(k_y - k_x)]\}\tau_1 - t'_{\pm,y}[\sin k_y + \sin(k_y - k_x)]\tau_2$ ,  $a_\tau^\pm = t_v \cos \varphi \sigma_1$ , and  $a_\tau^\pm = 2t_d \sin k_x \sigma_2$ . Here,  $\sigma_i$  and  $\tau_i$  ( $i = 1, 2, 3$ ) are two sets of Pauli matrices. The operators  $\sigma_0$  and  $\tau_0$  are the corresponding  $2 \times 2$  identity matrices. Also  $t_{\pm,\alpha} = (t_{\uparrow,\alpha} \pm t_{\downarrow,\alpha})/2$  and  $t'_{\pm,\alpha} = (t'_{\uparrow,\alpha} \pm t'_{\downarrow,\alpha})/2$ . Such a Laplacian matrix  $A$  has a close relation to the  $N$ -order Hamiltonian of lattice [Fig. 1(b)] which displays the nonreciprocal transport of the wave packet. Good agreement is shown where the dynamics of the voltages governed by the circuit matrix  $A$  corresponds to the evolution of the wave packet determined by the Hamiltonian; see Appendix C.

In the topological switch, the loss introduces non-Hermiticity, and the coupling in the  $x$  direction induces the skin effect, resulting in the eigenmode localization. Comparing with the quantum model, our designed circuits have a similar spectrum, eigenmode distribution, and topological mode governed by the Berry phase. The eigenvalues of matrix  $iA$  ( $iA|\phi\rangle = \lambda|\phi\rangle$ ) with certain parameters are presented in Fig. 2(a). In our calculation, the periodic boundary condition (PBC) is chosen along the  $x$  direction, and the open boundary condition (OBC) is taken along the  $y$  direction. The red and blue solid lines correspond to the eigenvalues of localized and bulk eigenmodes, respectively. The Berry phase related to the presence of edge states is

$$\gamma_n^y(k_x) = -\frac{1}{\pi} \text{Im} \oint_0^{2\pi} dk_y \langle u_n(k_x, k_y) | \partial_{k_y} | u_n(k_x, k_y) \rangle. \quad (4)$$

The state  $|u_n(k_x, k_y)\rangle$  is the  $n$ th eigenmode of the system  $iA(k_x, k_y)|u_n(k_x, k_y)\rangle = \varepsilon_n|u_n(k_x, k_y)\rangle$ . Considering that the PBC is chosen along the  $x$  direction and the OBC along the  $y$  direction, the average Berry phase is defined as  $\bar{\gamma}_n^y(k_x) = \sum_{k_x} \gamma_n^y(k_x)/N_x$ . It involves the Berry phase of the circuit Laplacian matrix with different  $k_x$ , which is proportional to the corner mode accumulation strength [54]. In Fig. 2(b), we provide the Berry phase from the eigenmode with the lowest eigenvalue for the nontrivial topology ( $\bar{\gamma} > 0$ ). Almost degenerate chiral edge modes (red curves) in Fig. 2(a) reflect the Chern topology, with their presence (or absence) at each  $k_x$  depending on whether the nearly quantized Berry phases are close to 1 or 0, and the average Berry phase  $\bar{\gamma}$  greater than zero shows the topological mode. At this time, the switch is on, and the reciprocity is broken such that non-reciprocal pumping dominates. For comparison, when some resistances are changed, the trivial topology can be obtained ( $\bar{\gamma} = 0$ ), and the switch is off, so the nonreciprocity with two sublattices favoring opposite directions is balanced and yields net reciprocity. We can also learn the results from the

between two nodes in the circuit. In Appendix B, we provide the dynamics of the voltages in the unit cell in detail.

When applying the Fourier transform to the Laplacian matrix  $A(x, y)$ , we have

eigenmode distribution. The eigenmode is the square of the modulus of the eigenstate of the matrix. Let  $\phi_m$  be the  $m$ th eigenstate of the circuit matrix, and the component at the  $n$ th node on the  $(x, y)$  unit cell is  $\phi_m(x, y, n)$ . The eigenmode on the unit cell  $\rho_{\text{sum}}(x, y) = \sum_m \sum_{n=1}^8 |\phi_m(x, y, n)|^2$  is the sum of the eigenmodes on the eight nodes of this unit cell. The eigenmode distributions  $\rho_{\text{sum}}(x, y)$  for different topologies are shown in Fig. 2(b) in a  $20 \times 10$  unit cell circuit. It is clearly found that  $\rho_{\text{sum}}$  is localized at two opposite corners, and the densities along  $x = 1$  and  $x = 20$  are obvious, while in the trivial case it is strongly clustered in the two of four corners, and the densities in the other two corner are almost 0. This kind of state distribution is useless for propagation. Moreover, the eigenmode distributions of three-dimensional circuits are shown in Fig. 2(c). Here we discuss two different three-dimensional circuit designs. One is the skin-topological-skin (skin-topo-skin) model, which displays the skin-topological (skin-topo) effect on the  $x$ - $y$  plane. We add a  $t_x$  connection in the  $z$  direction, so the skin effect along the  $z$  direction is implemented. For the skin-topo-skin model shown in the picture on the left in Fig. 2(c), the eigenmodes accumulate in the two corners. The other one is the skin-topological-topological (skin-topo-topo) model, which possesses topological-topological (topo-topo) modes on the  $y$ - $z$  plane, and  $t_x$  leads to the skin effect in the  $x$  direction. For the skin-topo-topo model shown in the picture on the right in Fig. 2(c), they accumulate in the four corners. The different eigenmode distribution results in different time evolution of the circuit.

### III. NUMERICAL RESULTS AND EXPERIMENTAL DEMONSTRATION OF TOPOLOGICAL SWITCH EFFECT

In the following, we provide numerical results for the topological switch effect. The value of capacitance in the circuit is taken as  $C = 1 \mu\text{F}$ . Different values of the resistances  $R_{j,k}$  in the op-amps are selected to accommodate with the ‘‘coupling’’ strengths shown in topological nontrivial and trivial cases in Fig. 2. In our simulation, the voltage is injected into the required nodes of the circuit, and then evolves in the whole circuit. Two different inputs of voltages  $V^R$  and  $V^L$  are shown for comparison. The case  $V^R$  describes that at the initial time ( $t = 0$  ms), only the voltage at the sublattice 1 of the position  $(x, y) = (20, 10)$  (top-right corner) in the circuit is  $V_{x=20, y=10, n=1} = 1$  V and the voltages at other nodes are zero. The case  $V^L$  denotes that at the initial time ( $t = 0$  ms), only the voltage at sublattice 1 of the position  $(x, y) = (1, 10)$  (top-left corner) in the circuit is  $V_{x=1, y=10, n=1} = 1$  V, and the

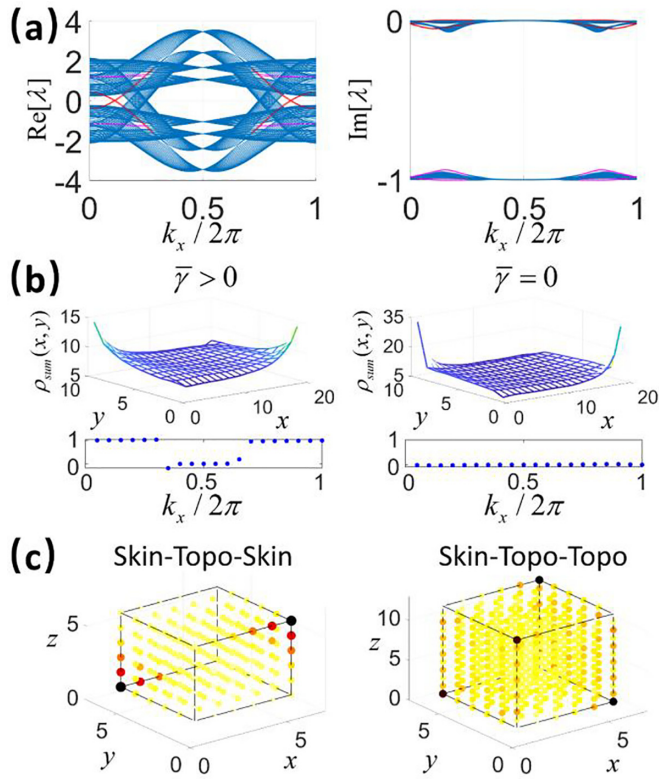


FIG. 2. Topological properties in the circuit Laplacian matrix. (a) Real and imaginary parts of the eigenvalues of the matrix  $iA$ . The coupling strengths between different sublattices  $\{g, t_{+,x}, t_{-,x}, t_{+,y}, t_{-,y}, t'_{+,y}, t'_{-,y}, \Delta_-, t_d, t_v\}$  are  $\{0.50, 0.39, 0.44, -0.11, -0.41, 0.45, 0.14, 1.25, -0.11, 0.19\}(\text{kF}^{-1} \Omega^{-1})$  and  $\varphi = \pi/2$ . The PBC (OBC) is chosen for the  $x$  ( $y$ ) direction. The eigenvalues of localized (bulk) eigenmodes are shown in red (blue). (b) The summation of probability distributions of eigenmodes  $\rho_{\text{sum}}(x, y)$  and Berry phase with different parameters. The circuit in the simulation contains  $20 \times 10$  unit cells. The parameters for  $\bar{\gamma} > 0$  follow those in (a), and the parameters for  $\bar{\gamma} = 0$  are changed to  $\{0.50, 0.06, 0.10, -0.57, -0.62, 0.36, 0.13, 0.76, -0.08, 0.32\}(\text{kF}^{-1} \Omega^{-1})$  and  $\varphi = \pi/2$ . (c) The eigenmodes  $\rho_{\text{sum}}$  for three-dimensional circuits. The topological boundary modes localize on the two edges while the skin modes localize on one edge. Therefore, the eigenmodes of the skin-topological-skin model accumulate at two corners while the eigenmodes of the skin-topological-topological model accumulate at four corners. The eigenmode distribution affects the time evolution of the circuit.

voltages at other nodes are zero. Then the circuit starts to evolve, and we explore the evolution of the electrical signal for the square of the voltages at the nodes,  $\rho_{x,y,n}(t) = V_{x,y,n}^2(t)$ . It corresponds to the probability density in the quantum model. We focus on the electrical signals on the unit cell, so we take  $\rho_{x,y}(t) = \sum_{n=1}^8 \rho_{x,y,n}(t)$  which summarizes the square of the voltages of the eight nodes in one unit cell at  $(x, y)$ . In Figs. 3(a) and 3(b), we provide the distributions of the square of the voltages in the circuit with  $t = 0, 6, 12$  (ms). The details of voltage distribution in different unit cells are provided in Appendix D.

As revealed above [Fig. 2(b)], when the circuit is topological nontrivial, the peak of the probability distribution of the

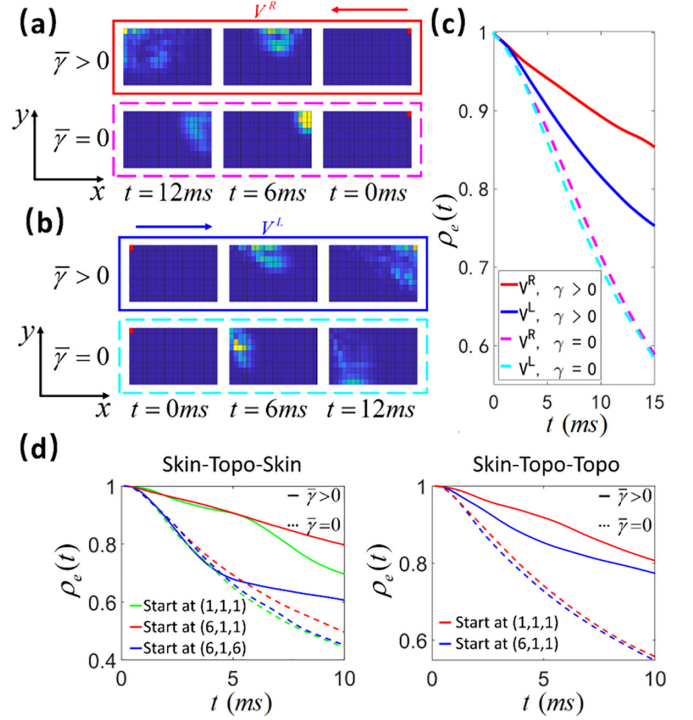


FIG. 3. Nonreciprocal transport of voltages in the circuit. (a) The electrical signal spreads from the top-right corner toward the left. (b) The electrical signal spreads from the top-left corner toward the right. In (a), (b), the parameters in the case with  $\bar{\gamma} > 0$  ( $\bar{\gamma} = 0$ ) are same as those in the left (right) of Fig. 2(b). The arrows indicate the direction of propagation of voltages. The circuit begins with the initial states  $V^R$  and  $V^L$  at  $t = 0$  ms. Due to the attenuation of the electrical signal, the square of the voltages at the beginning is larger than itself in the subsequent time, and we marked the initial square of the voltages in red. (c) The time evolution of the sum of the square of the voltages in the whole circuit  $\rho_e(t)$ . The initial state  $V^R$  with  $\bar{\gamma} > 0$  in red decays the least, indicative of topology-induced nonreciprocal transport. (d) The evolution of electrical signals in three-dimensional circuits. In the  $\bar{\gamma} > 0$  ( $\bar{\gamma} = 0$ ) case the nonreciprocal pumping is switched on (off). The starting coordinates  $(1, 1, 1)$  are the first unit cell in the  $x, y$ , and  $z$  directions. Only sublattice 1 of the starting unit cell has voltage 1 V while the other nodes in the circuit have voltage 0 V. These starting unit cells are all in the corner. With different starting coordinates, the electrical signals have different transmission results.

eigenmodes appears at the top-left corner of the circuit with  $(x, y) = (1, 10)$ . The nonreciprocal transport of the electrical signal can be found in the first row of Figs. 3(a) and 3(b). When the initial voltages start from the top-right corner ( $V^R$ ), the electrical signal is obvious at the top-left corner at  $t = 12$  ms, and only a few probabilities are found in the middle of the circuit; see the first row in Fig. 3(a). For comparison, when the initial voltages are at the top-left corner ( $V^L$ ), the electrical signal is less obvious at the top-right corner at  $t = 12$  ms, and more probabilities are found in the middle of the circuit; see the first row in Fig. 3(b). In this way, the topological switch is turned on, and the nonreciprocal transport of voltages is presented, while, when the circuit is topologically trivial, the transport along the edge of the circuit disappears, no matter

where the initial voltages start—from the top-left or -right corner. The second rows in Figs. 3(a) and 3(b) show such a phenomenon. Here, the topological switch is turned off. Therefore, the presence and the absence of the nonreciprocal transport of voltages is controlled by the topological switch.

We also show the sum of the squares of the voltages in the whole circuit  $\rho_e(t) = \sum_{x,y,n} \rho_{x,y,n}(t)$  with time; see Fig. 3(c). The decay rate of  $\rho_e(t)$  can show whether the switch turns on or off. Red and blue solid lines correspond to the evolution of  $\rho_e(t)$  when the topological switch is turned on, manifesting the nonreciprocal pumping. Magenta and cyan dashed lines indicate that the topological switch is turned off. It is shown that most of voltages are kept in the circuit when the topological switch is turned on, especially the case for the initial voltages starting from the top-right corner of the circuit (red solid line). Moreover, there exists an obvious difference of  $\rho_e(t)$  between the evolutions starting from the top-right and top-left corner. However, if the topological switch is turned off, lots of voltages are dissipated quickly with time. So the evolution of  $\rho_e(t)$  also indicates the topological properties in the circuit. Figure 3(d) demonstrates topological switches for three-dimensional circuits in Fig. 2(c). In Fig. 3(d), the size of the skin-topo-skin model is  $6 \times 6 \times 6$ , and the size of the skin-topo-topo model is  $6 \times 6 \times 12$ , so the starting coordinates are all on the corners. We use  $(x, y, z)$  to label the position of the unit cell in a three-dimensional circuit. For example,  $(1, 1, 1)$  means the first unit cell in the  $x, y$ , and  $z$  directions. When  $t = 0$  ms, only the voltage at sublattice 1 of the starting unit cell is 1 V, and the voltages at other nodes are 0 V. Solid lines correspond to topological cases while dashed lines correspond to trivial ones. Different colors correspond to different initial states. More details are provided in Appendix E.

To demonstrate experimentally the functioning of the topological switch, we physically construct the electric circuit. The unit cell of the electric circuit is provided in Fig. 4(a), and many cells are composed together to form the whole circuit. The red frame in Fig. 4(a) represents one unit cell, and the connections between different unit cells along the  $x$  direction and the  $y$  direction are shown in blue and orange frames, respectively. In the experiment, the op-amp LT1013 and the relay G6K-2F-Y are chosen. The value of capacitance is 1  $\mu\text{F}$ . Different resistances are chosen to implement the “coupling” between electric nodes. It is noted that such topological switches depend on hybrid skin-topological modes, and therefore similar results can be found for two- and three-dimensional circuits. We experimentally observed the topological switch in the two-dimensional circuit. The whole circuit contains  $3 \times 2$  unit cells and the nonreciprocal transport of the voltages can be observed clearly. The details of the whole circuit are shown in Appendix F. In Fig. 4(b), we provide the experimental results of  $\rho_e(t)$  with four different cases. Red and blue (magenta and cyan) dots correspond to the cases with the topological switch turned on (off). The initial voltage is injected into the top-right (-left) corner for red and magenta (blue and cyan) dots. It is found that when the topological switch is turned on, the dissipation of  $\rho_e(t)$  is very small with the initial voltage starting from the top-right corner. For comparison, when the topological switch is

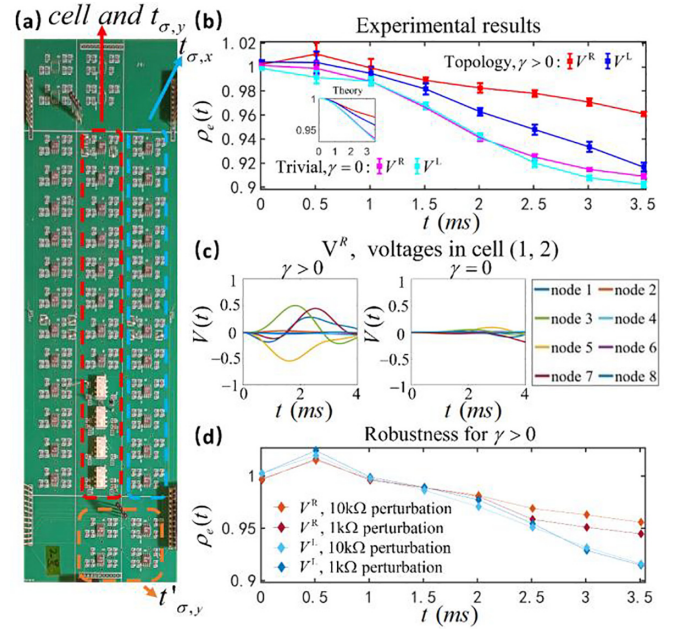


FIG. 4. Experimental realization of the topological switch. (a) The circuit realization for one unit cell: red frame, the unit cell; blue (orange) frame, the connection between cells along the  $x$  ( $y$ ) direction. (b) The evolution of the square of the voltages  $\rho_e(t)$  with different initial states and topology. The red dots ( $V^R$  with  $\gamma > 0$ ) decay the least, manifesting topology-induced nonreciprocal pumping. The magenta and cyan dots for the trivial case have the same decay rate, and the nonreciprocal pumping disappears. In the experiment, the whole circuit contains  $3 \times 2$  unit cells. For  $\gamma > 0$ , different resistances are chosen to make the coupling strengths between nodes  $\{g, t_{+,x}, t_{-,x}, t_{+,y}, t_{-,y}, t'_{+,y}, t'_{-,y}, \Delta_-, t_d, t_v\}$  become  $\{0.50, 0.45, 0.55, -0.00, -0.50, 0.50, 0.00, 1.00, -0.10, 0.10\}$  ( $\text{kF}^{-1} \Omega^{-1}$ ) and  $\varphi = \pi/2$ . For  $\gamma = 0$ , the “coupling” strengths become  $\{0.50, 0.03, 0.13, -0.45, -0.55, 0.33, 0.17, 1, -0.10, 0.32\}$  ( $\text{kF}^{-1} \Omega^{-1}$ ) and  $\varphi = \pi/2$ . The error bars are obtained from the average with data from 20 groups. The inset in the bottom left provides the simulation results. (c) The voltage evolution in  $(1, 2)$ . When  $\gamma > 0$ , the peak voltage means the successful transmission of the electrical signal, while when  $\gamma = 0$  the almost 0 V voltage means that the electrical signal cannot travel to this unit cell. (d) The decay of the square of the voltages with perturbations. The extra resistance connecting to the op-amp is chosen randomly. For dark red and blue (orange and cyan), the value of this resistance is chosen randomly in the range of 1 k $\Omega$  (10 k $\Omega$ ). With different perturbations,  $\rho_e(t)$  changes slightly which manifests the robustness.

turned off, the sum of voltages  $\rho_e(t)$  is dissipated quickly. The inset in the bottom left of Fig. 4(b) provides the simulation results with the same scale of circuit; they agree well with the experimental results. It is noted that the value of  $\rho_e(t)$  at the early time is slightly larger than 1, which might come from the op-amp. In Fig. 4(c), we exhibit the voltage evolution in  $(1, 2)$  with the initial state  $V^R$  beginning at the top-right corner. In the topological case ( $\gamma > 0$ ), an electrical signal can propagate to the top-left while it cannot in the trivial case ( $\gamma = 0$ ). More experimental details and error analysis are shown in Appendix G.

#### IV. ROBUSTNESS

Moreover, to verify the topological properties of a switch, the perturbation is introduced into the circuit. As an example, we randomly choose ten to 20 resistors, and connect them in parallel with 10 k $\Omega$  resistors. We repeat this behavior ten times and observe the average results. We also perform similar operations using 1 k $\Omega$  resistors. When the topological switch is turned on, the sum of the squares of the voltages with perturbation is shown in Fig. 4(d). With different perturbations,  $\rho_e(t)$  changes slightly. In these cases, the topological mode still exists, and the difference of  $\rho_e(t)$  between the decay of  $V^R$  and  $V^L$  exists. All of these indicate the existence of the nonreciprocal transport of voltages, which demonstrates the robustness of this switch.

#### V. SUMMARY

In summary, we experimentally demonstrated a topological switch on the non-Hermitian skin effect in our designed circuit. The nonreciprocal transport of voltages has been uncovered when the topological switch is turned on. Even for a small circuit, the performance as a topological switch is evident. We have also experimentally constructed an electric circuit to implement the topological switch and demonstrated the nonreciprocal transport of voltages. Furthermore, the robust property of the topological switch has also been demonstrated when a small perturbation is introduced. This means that the electrical signal propagations can be controlled very finely by designing the circuit networks, and the present work may have potential applications in the field of integrated circuit design.

#### ACKNOWLEDGEMENTS

This work was supported by the National Key R & D Program of China under Grant No. 2022YFA1404900 and the National Natural Science Foundation of China (Grants No. 12234004 and No. 12104041).

#### APPENDIX A: PROPERTIES OF LUMPED OPERATIONAL AMPLIFIER STRUCTURES

In our design, the op-amp is used to realize the topological switch. Here, we give the details of the op-amp.

In Fig. 5, the details of the op-amp structure are shown. The main module in the op-amp is the negative impedance converter (INIC). In the INIC, the inverting input voltage is equal to the noninverting input voltage  $V_2 = V_j$ , and the inverting and noninverting input currents are zero  $I_{op1,+} = I_{op1,-} = 0$ . Thus  $I_{j1} = \frac{V_j - V_1}{R_0} = \frac{V_2 - V_1}{R_0} = I_{21} = I_{k2} = \frac{V_k - V_2}{R_{jk}} = \frac{V_j - V_k}{-R_{jk}}$ , and the current flowing through the INIC is equal in magnitude but opposite in direction. In this way, the INIC can be equivalent to an ‘‘effective resistance’’ connecting node  $j$  to node  $k$ ,  $R'_{jk}$  and  $R'_{kj}$ , which also determines the values of  $A_{jk}$  and  $A_{kj}$  in the circuit Laplacian matrix. According to the circuit equation, the INIC is supposed to change the values of the diagonal terms  $A_{jj}$  and  $A_{kk}$ . Therefore, we add a grounding part to each node, which is used to eliminate this extra diagonal term in

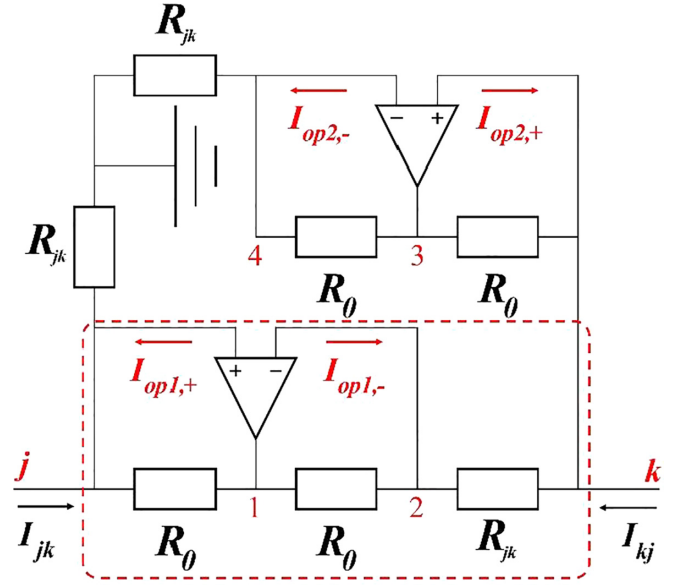


FIG. 5. The op-amp structure. The node at the left of the structure is the node  $j$ , and the node at the right of structure is node  $k$ . The main module, called the negative impedance converter (INIC), is marked with a red box, while the rest is the grounding module. The resistance  $R_0$  is constant, while the resistance  $R_{jk}$  varies with the parameters.

the circuit Laplacian matrix. Now in the op-amp structure, we have

$$\begin{aligned} I_{jk} &= \frac{V_j}{R_{jk}} + \frac{V_j - V_1}{R_0} = \frac{V_j}{R_{jk}} + \frac{V_2 - V_1}{R_0} = \frac{V_j}{R_{jk}} + I_{21} \\ &= \frac{V_j}{R_{jk}} + I_{k2} + I_{op1,-} = \frac{V_j}{R_{jk}} + \frac{V_k - V_2}{R_{jk}} + 0 = \frac{V_k}{R_{jk}} \\ &= \frac{V_k}{R'_{jk}}. \end{aligned} \quad (A1)$$

In a similar way, we have  $I_{kj} = -\frac{V_j}{R_{jk}} = \frac{V_j}{R'_{kj}}$ , so we have  $R'_{kj} = -R'_{jk}$ , which means the ‘‘effective resistances’’ between  $R'_{jk}$  (from node  $j$  to  $k$ ) and  $R'_{kj}$  (from node  $k$  to  $j$ ) are opposite. Compared with the simple INIC, the value of the diagonal term in the circuit matrix is not changed with the addition of these grounding parts.

#### APPENDIX B: EQUATIONS OF VOLTAGES IN THE CIRCUIT DESIGN

In Fig. 1 in the main text, we have provided the circuit design. Here, we provide the dynamics of voltages in the circuit. In our design, each unit cell contains eight sublattices (nodes). We label different unit cells with different positions  $(x, y)$ , and the different sublattices are expressed from 1 to 8 as shown in Fig. 1(a). The dynamics of the voltages for these sublattices are satisfied by Kirchhoff

equations as

$$\begin{aligned}
-C \frac{dV_{x,y,1}}{dt} = & t_v \sin \varphi V_{x,y,2} + \Delta_- V_{x,y,3} + t_v \cos \varphi V_{x,y,4} - (t_{+,y} + t_{-,y}) V_{x,y,7} \\
& - t_d V_{x-1,y,4} + t_d V_{x+1,y,4} - (t_{+,x} + t_{-,x}) V_{x-1,y,3} - (t_{+,x} + t_{-,x}) V_{x+1,y,3} \\
& - (t'_{+,y} + t'_{-,y}) V_{x,y+1,7} - (t'_{+,y} + t'_{-,y}) V_{x-1,y+1,7},
\end{aligned} \tag{B1}$$

$$\begin{aligned}
-C \frac{dV_{x,y,2}}{dt} = & -t_v \sin \varphi V_{x,y,1} + 2g V_{x,y,2} + t_v \cos \varphi V_{x,y,3} - \Delta_- V_{x,y,4} - (t_{+,y} - t_{-,y}) V_{x,y,8} \\
& + t_d V_{x-1,y,3} - t_d V_{x+1,y,3} + (t_{+,x} - t_{-,x}) V_{x-1,y,4} + (t_{+,x} - t_{-,x}) V_{x+1,y,4} \\
& - (t'_{+,y} - t'_{-,y}) V_{x,y+1,8} - (t'_{+,y} - t'_{-,y}) V_{x-1,y+1,8},
\end{aligned} \tag{B2}$$

$$\begin{aligned}
-C \frac{dV_{x,y,3}}{dt} = & -\Delta_- V_{x,y,1} - t_v \cos \varphi V_{x,y,2} + t_v \sin \varphi V_{x,y,4} + (t_{+,y} + t_{-,y}) V_{x,y,5} \\
& + t_d V_{x-1,y,2} - t_d V_{x+1,y,2} + (t_{+,x} + t_{-,x}) V_{x-1,y,1} + (t_{+,x} + t_{-,x}) V_{x+1,y,1} \\
& + (t'_{+,y} + t'_{-,y}) V_{x,y+1,5} + (t'_{+,y} + t'_{-,y}) V_{x-1,y+1,5},
\end{aligned} \tag{B3}$$

$$\begin{aligned}
-C \frac{dV_{x,y,4}}{dt} = & -t_v \cos \varphi V_{x,y,1} + \Delta_- V_{x,y,2} - t_v \sin \varphi V_{x,y,3} + 2g V_{x,y,4} + (t_{+,y} - t_{-,y}) V_{x,y,6} \\
& - t_d V_{x-1,y,1} + t_d V_{x+1,y,1} + (t_{+,x} - t_{-,x}) V_{x-1,y,2} + (t_{+,x} - t_{-,x}) V_{x+1,y,2} \\
& + (t'_{+,y} + t'_{-,y}) V_{x,y+1,6} + (t'_{+,y} + t'_{-,y}) V_{x-1,y+1,6},
\end{aligned} \tag{B4}$$

$$\begin{aligned}
-C \frac{dV_{x,y,5}}{dt} = & -(t_{+,y} + t_{-,y}) V_{x,y,3} - t_v \sin \varphi V_{x,y,6} + \Delta_- V_{x,y,7} - t_v \cos \varphi V_{x,y,8} \\
& - t_d V_{x-1,y,8} + t_d V_{x+1,y,8} - (t_{+,x} + t_{-,x}) V_{x-1,y,7} - (t_{+,x} + t_{-,x}) V_{x+1,y,7} \\
& - (t'_{+,y} + t'_{-,y}) V_{x,y-1,3} - (t'_{+,y} + t'_{-,y}) V_{x+1,y-1,3},
\end{aligned} \tag{B5}$$

$$\begin{aligned}
-C \frac{dV_{x,y,6}}{dt} = & -(t_{+,y} - t_{-,y}) V_{x,y,4} + t_v \sin \varphi V_{x,y,5} + 2g V_{x,y,6} - t_v \cos \varphi V_{x,y,7} - \Delta_- V_{x,y,8} \\
& + t_d V_{x-1,y,7} - t_d V_{x+1,y,7} - (t_{+,x} - t_{-,x}) V_{x-1,y,8} - (t_{+,x} - t_{-,x}) V_{x+1,y,8} \\
& - (t'_{+,y} - t'_{-,y}) V_{x,y-1,4} - (t'_{+,y} - t'_{-,y}) V_{x+1,y-1,4},
\end{aligned} \tag{B6}$$

$$\begin{aligned}
-C \frac{dV_{x,y,7}}{dt} = & (t_{+,x} + t_{-,x}) V_{x,y,1} - \Delta_- V_{x,y,5} + t_v \cos \varphi V_{x,y,6} - t_v \sin \varphi V_{x,y,8} \\
& + t_d V_{x-1,y,6} - t_d V_{x+1,y,6} + (t_{+,x} + t_{-,x}) V_{x-1,y,5} + (t_{+,x} + t_{-,x}) V_{x+1,y,5} \\
& + (t'_{+,y} + t'_{-,y}) V_{x,y-1,1} + (t'_{+,y} + t'_{-,y}) V_{x+1,y-1,1},
\end{aligned} \tag{B7}$$

$$\begin{aligned}
-C \frac{dV_{x,y,8}}{dt} = & (t_{+,y} - t_{-,y}) V_{x,y,2} + t_v \cos \varphi V_{x,y,5} + \Delta_- V_{x,y,6} + t_v \sin \varphi V_{x,y,7} + 2g V_{x,y,8} \\
& - t_d V_{x-1,y,5} + t_d V_{x+1,y,5} + (t_{+,x} - t_{-,x}) V_{x-1,y,6} + (t_{+,x} - t_{-,x}) V_{x+1,y,6} \\
& + (t'_{+,y} - t'_{-,y}) V_{x,y-1,2} + (t'_{+,y} - t'_{-,y}) V_{x+1,y-1,2}.
\end{aligned} \tag{B8}$$

The voltages at the sublattices of each unit cell satisfy these eight equations. If we use the column vector  $|V(t)\rangle$  to represent the voltages in the whole circuit, we can have the equation involving the circuit Laplacian matrix  $A$ ,  $i \frac{d|V(t)\rangle}{dt} = iA|V(t)\rangle$ . Here as a result, we exhibit the numerical results of the voltage evolution along the boundaries; this behavior is essentially determined by these equations above. See Fig. 6.

### APPENDIX C: CORRESPONDENCE BETWEEN THE CIRCUIT AND THE LATTICE

The dynamics of the voltages are expressed as the equation  $i \frac{d|V(t)\rangle}{dt} = iA|V(t)\rangle$ . In the following,

we show the correspondence between such dynamics of voltages and quantum evolution of wave packets.

The quantum evolution of the wave packet  $|\varphi\rangle$  satisfies the Schrödinger equation  $H|\varphi\rangle = i \frac{\partial}{\partial t} |\varphi\rangle$ . When the complex conjugate operation is applied to this evolution, we have  $H^*|\varphi\rangle^* = -i \frac{\partial}{\partial t} |\varphi\rangle^*$ . The superscript “\*” denotes the complex conjugate operation. By combining these two equations, we have the form  $\begin{bmatrix} H & 0 \\ 0 & -H^* \end{bmatrix} \frac{1}{\sqrt{2}} \begin{pmatrix} |\varphi\rangle \\ |\varphi\rangle^* \end{pmatrix} = i \frac{\partial}{\partial t} \frac{1}{\sqrt{2}} \begin{pmatrix} |\varphi\rangle \\ |\varphi\rangle^* \end{pmatrix}$ .

Consider the unitary transformation  $U = \frac{1}{\sqrt{2}} \begin{bmatrix} 1 & -i \\ i & 1 \end{bmatrix} \otimes I$ , where the operator  $I$  is the identity matrix whose dimension is the same as the Hamiltonian  $H$ ; the equation now

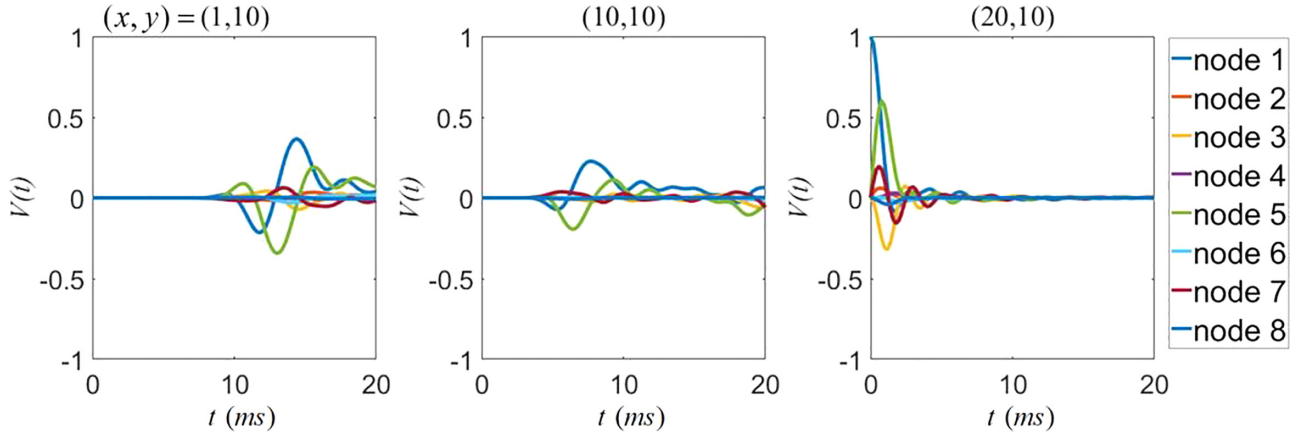


FIG. 6. The voltage evolution of the unit cell.

becomes

$$U^\dagger \begin{bmatrix} H & \\ & -H^* \end{bmatrix} U U^\dagger \frac{1}{\sqrt{2}} \begin{pmatrix} |\varphi\rangle \\ |\varphi\rangle^* \end{pmatrix} = U^\dagger i \frac{\partial}{\partial t} \frac{1}{\sqrt{2}} \begin{pmatrix} |\varphi\rangle \\ |\varphi\rangle^* \end{pmatrix}, \quad (\text{C1})$$

or

$$i \begin{bmatrix} \text{Im}[H] & -\text{Re}[H] \\ \text{Re}[H] & \text{Im}[H] \end{bmatrix} \begin{pmatrix} \text{Re}[|\varphi\rangle] \\ -\text{Im}[|\varphi\rangle] \end{pmatrix} = i \frac{\partial}{\partial t} \begin{pmatrix} \text{Re}[|\varphi\rangle] \\ -\text{Im}[|\varphi\rangle] \end{pmatrix}, \quad (\text{C2})$$

where  $\text{Re}[H] = \frac{1}{\sqrt{2}}(H + H^*)$  and  $\text{Im}[H] = \frac{-i}{\sqrt{2}}(H - H^*)$ . So far,  $H$  can be any matrix.

As we mentioned in the main text, the circuit equation is  $iA|V(t)\rangle = i \frac{d|V(t)\rangle}{dt}$ . Here  $|V(t)\rangle = [V_1(t), V_2(t), \dots, V_{2N}(t)]^T$  is the column vector consisting of the voltages at all  $2N$  nodes in the circuit, where  $V_j(t)$  is the voltage at the node  $j$ , and the operator  $T$  represents the transpose operator. In this way, the circuit Laplacian matrix is assumed to have the form  $A = \begin{bmatrix} \text{Im}[h_{2D}] & -\text{Re}[h_{2D}] \\ \text{Re}[h_{2D}] & \text{Im}[h_{2D}] \end{bmatrix}$ , where we take  $H = h_{2D}$  as the Hamiltonian of the corresponding quantum system, and  $h_{2D}$  is an  $N \times N$  matrix. We also apply the Fourier transform to  $h_{2D}$ ,  $h_{2D}(k_x, k_y) = \int dx dy h_{2D}(x, y) e^{i(k_x x + k_y y)}$ , and obtain the expression of  $h_{2D}(k_x, k_y) = h_{2D}(\vec{k}) = h_\sigma^+ \sigma_0 + h_\sigma^- \sigma_3 + h_\tau^+ \tau_0 +$

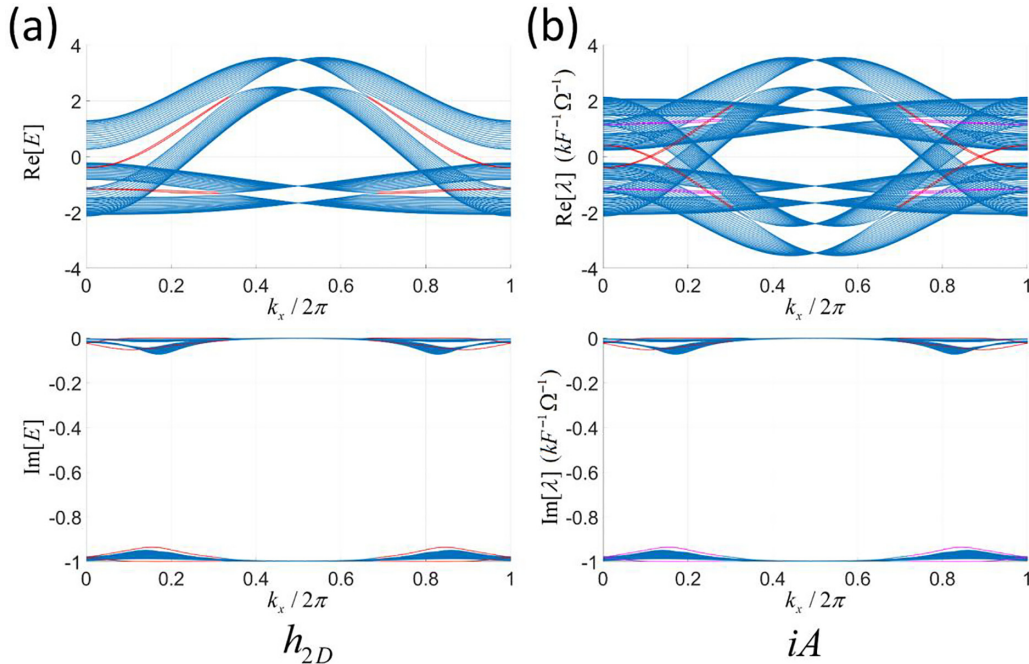


FIG. 7. The spectrum of Hamiltonian  $h_{2D}$  and circuit matrix  $iA$ . (a) Real and imaginary parts of the spectrum for  $h_{2D}$ . The periodic boundary condition (PBC) is chosen along the  $x$  direction, and the open boundary condition (OBC) is chosen along the  $y$  direction. The value of coupling parameters  $\{g, t_{+,x}, t_{-,x}, t_{+,y}, t_{-,y}, t'_{+,y}, t'_{-,y}, \Delta_-, t_d, t_v\}$  in the Hamiltonian  $h_{2D}$  are  $\{0.50, 0.39, 0.44, -0.11, -0.41, 0.45, 0.14, 1.25, -0.11, 0.19\}$  and  $\varphi = \pi/2$ . (b) Real and imaginary parts of the spectrum for  $iA$ . The PBC is chosen along the  $x$  direction, and the OBC is chosen along the  $y$  direction of the circuit. The value of the parameters in the circuit Laplacian matrix  $A$  are the same as in Fig. 2 in the main text. In (a), (b), red (blue) solid lines represent the localized (bulk) eigenmodes of the system.



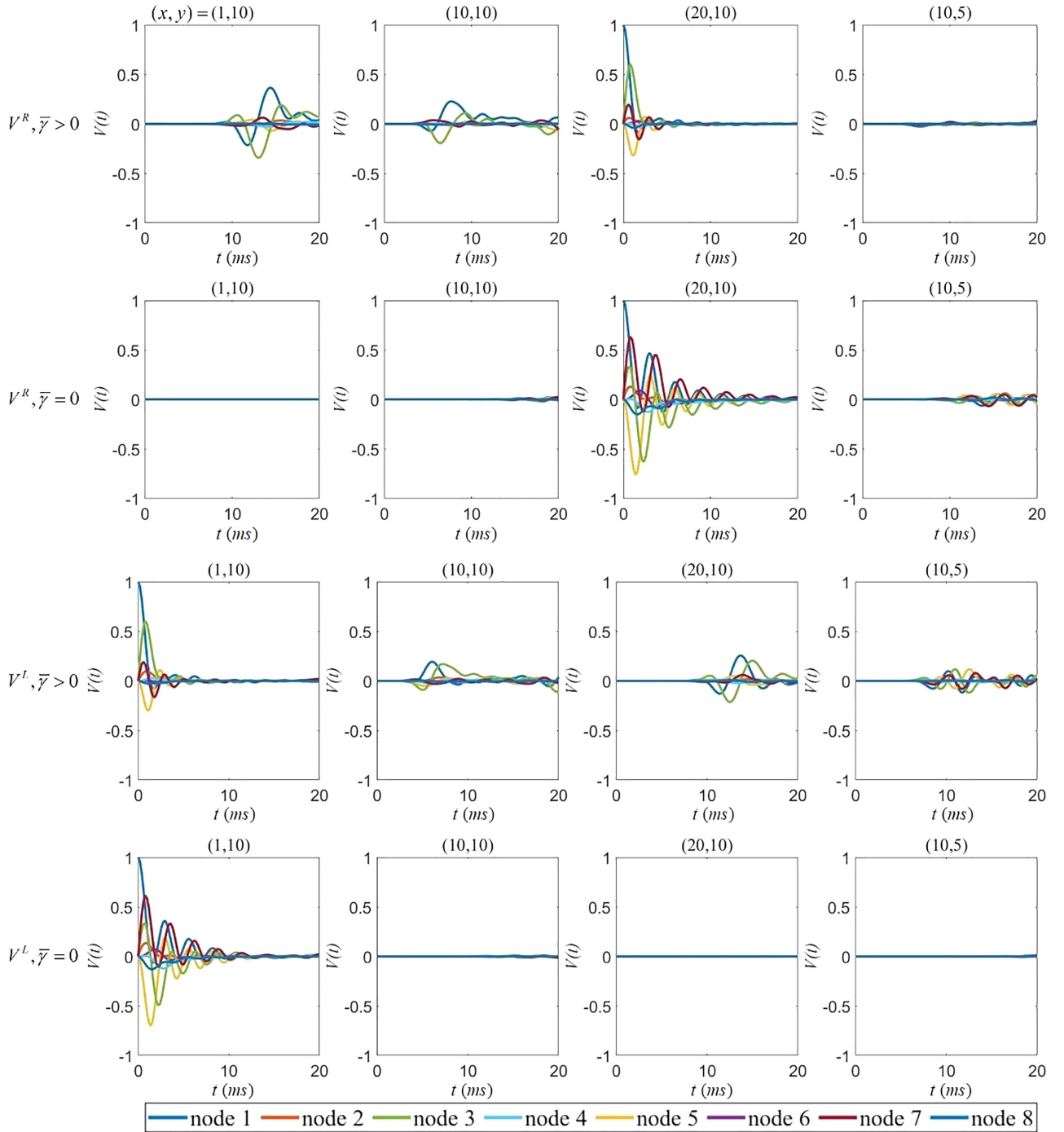


FIG. 8. The dynamics of voltages at four different unit cells in the simulation. In the topological case ( $\gamma > 0$ ), the electrical signal can propagate along the boundaries, and the nonreciprocal pumping can be quantified through the decaying of the total electrical signal  $\rho_e(t)$  in the main text. But in the trivial case ( $\gamma = 0$ ), the voltages in the boundaries are almost 0.

$h_{\tau}^{-} \tau_3$ , with

$$\begin{aligned}
 h_{\sigma}^{\pm} &= -(2t_{\pm,x} \cos k_x - \Delta_{\pm} \pm ig) \tau_0 \\
 &\quad - \{t_{\pm,y} + t'_{\pm,y} [\cos k_y + \cos(k_y - k_x)]\} \tau_1 \\
 &\quad - t'_{\pm,y} [\sin k_y + \sin(k_y - k_x)] \tau_2, \\
 h_{\tau}^{-} &= (t_v \cos \varphi) \sigma_1 + (t_v \sin \varphi) \sigma_2, \\
 h_{\tau}^{+} &= (2t_d \sin k_x) \sigma_2.
 \end{aligned}
 \tag{C3}$$

This is the Hamiltonian for Fig. 1(b). Therefore, if we provide the appropriate initial voltages in the circuit, we can show the quantum evolution governed by this Hamiltonian. The eigenvalues of  $h_{2D}$  are shown in Fig. 7, which have similar topological eigenmodes as those in the circuit Laplacian matrix  $iA$ . The difference between Figs. 7(a) and 7(b) comes from the similarity that  $iA = U^{\dagger} [t_{h_{2D}}^{-h_{2D}^*}] U$ , where  $U = \frac{1}{\sqrt{2}} \begin{bmatrix} 1 & -i \\ 1 & i \end{bmatrix} \otimes I$  and the operator  $I$  is the identity matrix whose

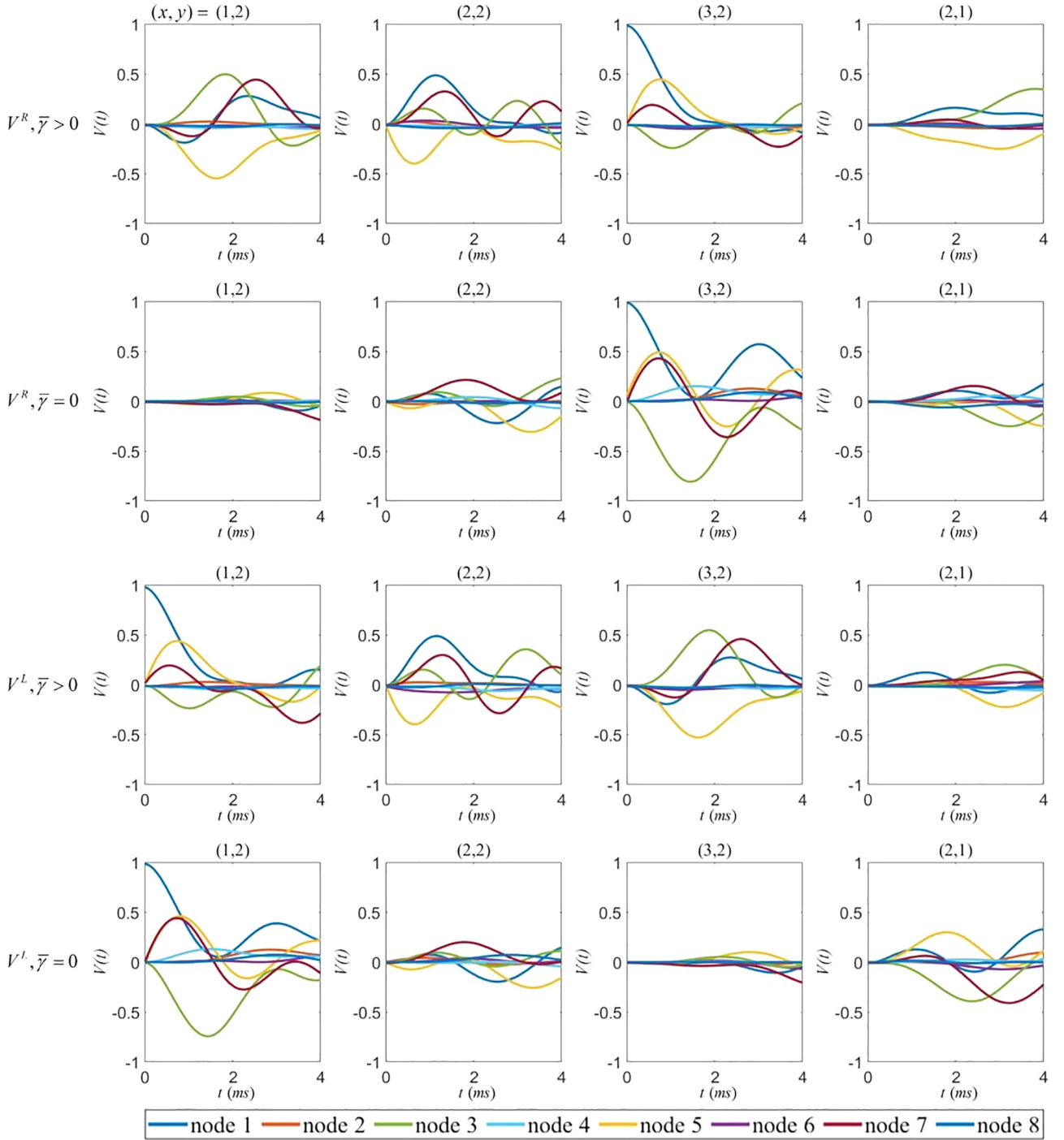


FIG. 9. The dynamics of voltages at four different unit cells in the experiment. In the topological case ( $\gamma > 0$ ), the electrical signal can propagate along the boundaries. But in the trivial case ( $\gamma = 0$ ), the voltages in the boundaries are close to 0.

dimension is the same as the Hamiltonian  $h_{2D}$ . Although the circuit system contains no imaginary number, we can simulate the real and imaginary parts of the quantum evolution by the real voltage in the circuit based on the similarity. In this way, the correspondence between the dynamics of the voltages and the quantum evolution of the wave packets is established.

As shown in Fig. 7, we can find that the topological eigenmodes appear in the Hamiltonian  $h_{2D}$  [red solid lines in Fig. 7(a)] under certain parameters. Although the distribution

of the spectra shows some differences, the topological eigenmodes are still found in the red solid lines [Fig. 7(b)] when referring to the spectrum of  $iA$ .

#### APPENDIX D: DYNAMICS OF VOLTAGES AT DIFFERENT UNIT CELLS

The nonreciprocal transport of voltages has been shown in the main text. In our discussion, the nonreciprocal transport can be found when the topological switch is turned on, and

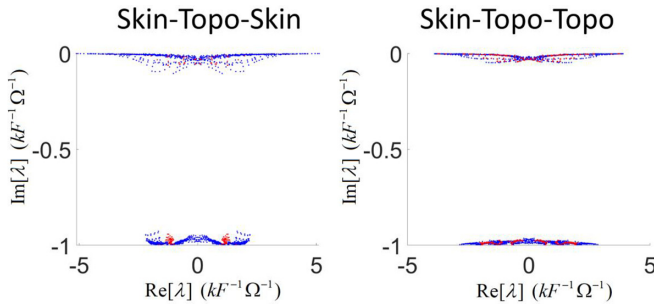


FIG. 10. The eigenvalue of the three-dimensional circuit.

there is no such nonreciprocal transport when the switch is turned off. Here, we provide the evolution details of some unit cells during the nonreciprocal transport. Four different unit cells are chosen to show the evolution. The positions of these unit cells in the circuit are  $(x, y) = (1, 10)$  (top-left corner),  $(x, y) = (10, 10)$  (middle of the top),  $(x, y) = (20, 10)$  (top-right corner), and  $(x, y) = (10, 5)$  (middle of the circuit).

When the topological switch is turned on, the voltage starting from the top-right corner (the first row in Fig. 8) is found at the top-left corner with time, obviously. For comparison, when the switch is turned off, the voltage starting from the top-right corner (the second row in Fig. 8) is hardly found at

the top-left corner with time. Most of the voltages are found in the bulk of the circuit. In the third and fourth rows of Fig. 8, the voltages start from the top-left corner. When the topological switch is turned on, the voltage can be found at the top-right corner with time (the third row in Fig. 8). The amplitudes of the voltages are smaller than those in the first row while, when the switch is turned off, no voltage can be found at the top-right corner, and the transport of the voltages is not along the edge of the circuit.

We also provide the dynamics of the voltages in the experiment. Four different unit cells are chosen and the positions are  $(x, y) = (1, 2)$  (top-left corner),  $(x, y) = (2, 2)$  (middle of the top),  $(x, y) = (3, 2)$  (top-right corner), and  $(x, y) = (2, 1)$  (bottom of the circuit).

In our experiment, we choose the circuit with a small size. When the topological switch is turned on, we find that most of the voltages can be found along the top (the first and third rows in Fig. 9). When the topological switch is turned off, the voltages at the bottom become obvious (the rightmost panels in the second and fourth rows in Fig. 9).

#### APPENDIX E: DYNAMICS OF THREE-DIMENSIONAL CIRCUIT

The three-dimensional circuit is based on the two-dimensional circuit, so that they have similar Laplacian matrices,

$$A(k_x, k_y, k_z) = \begin{bmatrix} g(\sigma_3 - \sigma_0)\tau_0 - it_v \sin \varphi \sigma_2 \tau_3 & -[\sigma_0 a_\sigma^+ + \sigma_3 a_\sigma^- + a_\tau^+ \tau_0 + a_\tau^- \tau_3] \\ \sigma_0 a_\sigma^+ + \sigma_3 a_\sigma^- + a_\tau^+ \tau_0 + a_\tau^- \tau_3 & g(\sigma_3 - \sigma_0)\tau_0 - it_v \sin \varphi \sigma_2 \tau_3 \end{bmatrix}, \quad (\text{E1})$$

where for the skin-topo-skin model,

$$\begin{aligned} a_\sigma^\pm &= -(2t_{\pm,x} \cos k_x + 2t_{\pm,x} \cos k_z - \Delta_\pm)\tau_0 \\ &\quad - \{t_{\pm,y} + t'_{\pm,y}[\cos k_y + \cos(k_y - k_x) + \cos(k_y - k_z)]\}\tau_1 \\ &\quad - t'_{\pm,y}[\sin k_y + \sin(k_y - k_x) + \sin(k_y - k_z)]\tau_2, \\ a_\tau^- &= t_v \cos \varphi \sigma_1, \\ a_\tau^+ &= 2t_d(\sin k_x + \sin k_z)\sigma_2, \end{aligned} \quad (\text{E2})$$

and for the skin-topo-topo model,

$$\begin{aligned} a_\sigma^\pm &= -(2t_{\pm,x} \cos k_x - \Delta_\pm)\tau_0 \\ &\quad - \{t_{\pm,y} + t'_{\pm,y}[\cos k_y + \cos(k_y - k_x) \\ &\quad + \cos k_z + \cos(k_z - k_x)]\}\tau_1 \\ &\quad - t'_{\pm,y}[\sin k_y + \sin(k_y - k_x) + \sin k_z + \sin(k_z - k_x)]\tau_2, \\ a_\tau^- &= t_v \cos \varphi \sigma_1, \\ a_\tau^+ &= 2t_d \sin k_x \sigma_2. \end{aligned} \quad (\text{E3})$$

Here we present the spectrum of three-dimensional circuits in Fig. 10 and the dynamics of them in Fig. 11. For the  $\bar{\gamma} > 0$  ( $\bar{\gamma} = 0$ ) case, the nonreciprocal pumping is switched on (off) along the direction displaying the skin effect.

#### APPENDIX F: ASSEMBLY OF UNIT CELLS IN THE ELECTRIC CIRCUIT

A photo of the assembly of the unit cells in the electric circuit is shown in Fig. 12. The whole circuit contains  $3 \times 2$  unit cells. In Fig. 12, we provide the whole electric circuit in the experiment. It consists of six printed circuit boards (PCBs) where each PCB denotes one unit cell. Along the  $x$  direction, the unit cell is connected to the pin header through the op-amp. The type of op-amp is LT1013, in which the value of  $R_0 = 1 \text{ k}\Omega$ . The different values of  $R_{jk}$  are chosen according to the design. Three different  $R_{jk}$ ,  $R_{jk} = 1 \text{ k}\Omega$ ,  $R_{jk} = 6.2 \text{ k}\Omega$ , and  $R_{jk} = 10 \text{ k}\Omega$ , are selected, respectively. Along the  $y$  direction, the unit cell is also connected to the pin header by the op-amp. The type of such op-amps is also LT1013, and  $R_0 = 1 \text{ k}\Omega$ . Two different  $R_{jk}$ ,  $R_{jk} = 2 \text{ k}\Omega$  and  $R_{jk} = 6.2 \text{ k}\Omega$ , are chosen corresponding to the two kinds of couplings along the  $y$  direction. At the boundary of the circuit, the op-amp is removed or grounded to screen the disturbance on the circuit.

#### APPENDIX G: EXPERIMENTAL DETAILS AND ERROR ANALYSIS IN THE CIRCUIT

In the circuit, we use the op-amp LT1013 and the relay G6K-2F-Y. The value of the capacitor is  $1 \text{ }\mu\text{F}$ , and the

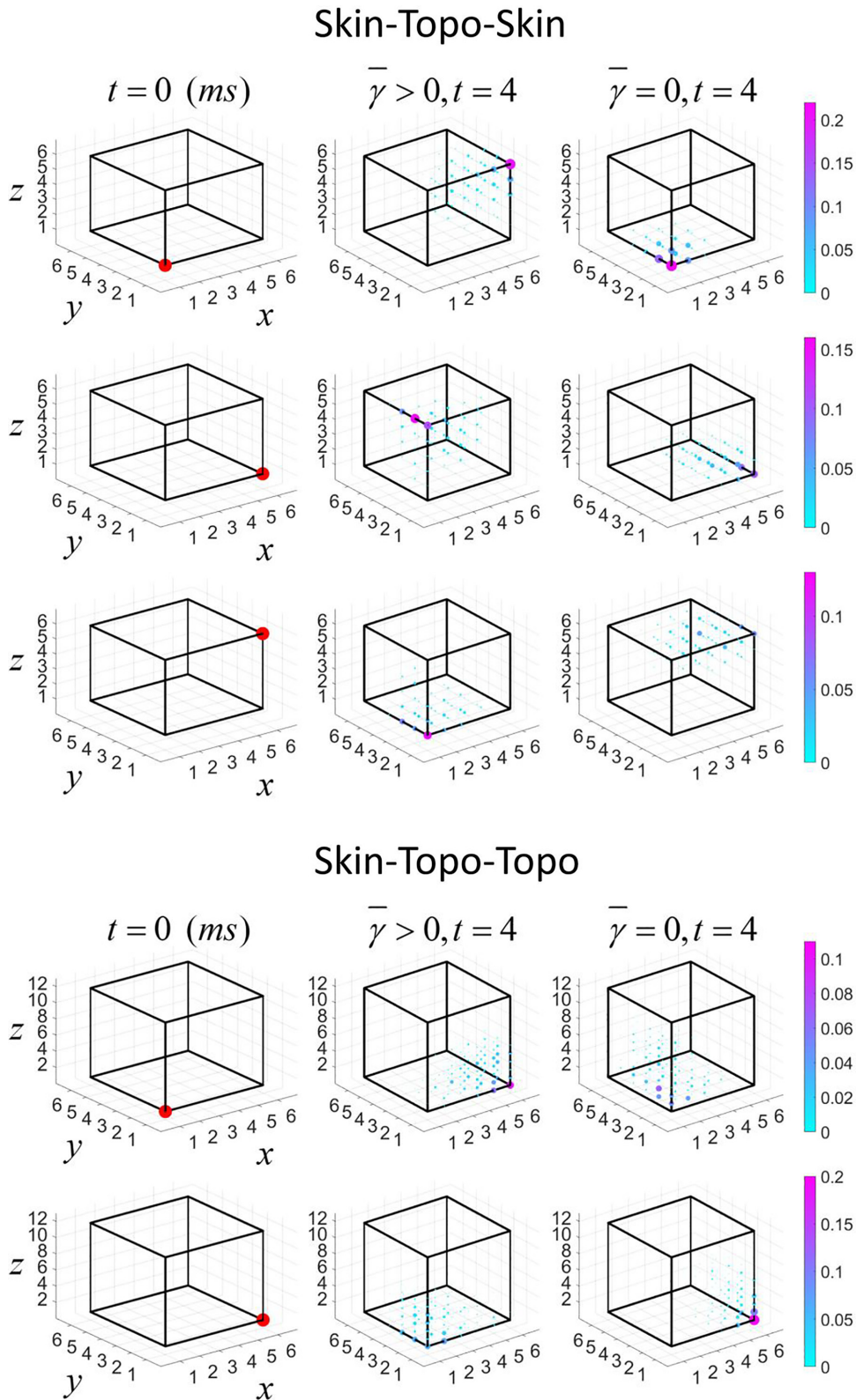


FIG. 11. The dynamics of three-dimensional circuits. We present the distribution of the electrical signal in the whole circuit at  $t = 4$  ms. The left column is the square of the voltages at initial time, and the next two columns are the evolution results for the  $\bar{\gamma} > 0$  case (middle column) and the  $\bar{\gamma} = 0$  case (right column). At the beginning, the electrical signal exists at one unit cell. The electrical signal for the  $\bar{\gamma} > 0$  case travels along the direction displaying the skin effect, while for the case with  $\bar{\gamma} = 0$  it does not. Due to the attenuation of the electrical signal, the square of the voltages at the beginning is larger than itself in the subsequent time, so we mark the initial square of the voltages in red. For the skin-topo-skin case, the initial voltage locates at the position  $(x, y, z) = (1,1,1)$ ,  $(6,1,1)$ , and  $(6,1,6)$  from top to bottom; for the skin-topo-topo case, the initial voltage locates at the position  $(x, y, z) = (1,1,1)$  and  $(6,1,1)$  from top to bottom.

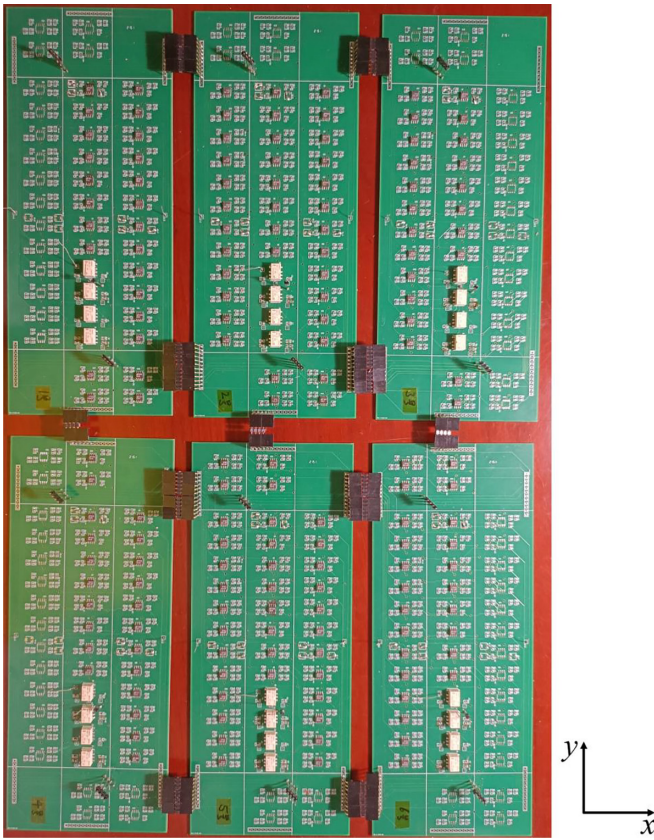


FIG. 12. The whole electric circuit in the experiment.

resistances are taken as 1, 2, 6.2, and 10 k $\Omega$ . In the simulation, when the topological switch is turned on, the resistances  $R_{jk}$  of the op-amp LT1063 in the unit cell are chosen as  $R_{12} = 0.8$  k $\Omega$ ,  $R_{13} = +\infty$  (which is realized by the open circuit),  $R_{14} = 5$  k $\Omega$ ,  $R_{17} = 2$  k $\Omega$ , and  $R_{28} = 3$  k $\Omega$ . Along the  $y$  direction, the op-amp is used to connect different unit cells. The resistance  $R_{jk}$  of the op-amp LT1063 is chosen as  $R_{17} = 2$  k $\Omega$  and  $R_{28} = 3$  k $\Omega$ . Along the  $x$  direction, the op-amp is used to connect different unit cells. The resistance  $R_{jk}$  of the op-amp LT1063 is chosen as  $R_{13} = 1.3$  k $\Omega$ ,  $R_{14} = 10$  k $\Omega$ , and  $R_{23} = 20$  k $\Omega$ . For comparison, when the topological switch is turned off, the resistance  $R_{jk}$  of the op-amp LT1063 in the unit cell is chosen as  $R_{12} = 1.3$  k $\Omega$ ,  $R_{13} = +\infty$  (which is realized by the open circuit),  $R_{14} = 3$  k $\Omega$ ,  $R_{17} = 20$  k $\Omega$ , and  $R_{28} = 0.8$  k $\Omega$ . Along the  $y$  direction, the op-amp is used to connect different unit cells. The resistance  $R_{jk}$  of the op-amp LT1063 is chosen as  $R_{17} = 2$  k $\Omega$  and  $R_{28} = 4$  k $\Omega$ . Along the  $x$  direction, the op-amp is also used to connect different unit cells. The resistance  $R_{jk}$  of the op-amp LT1063 is chosen as  $R_{13} = 6.2$  k $\Omega$ ,  $R_{14} = 10$  k $\Omega$ , and  $R_{23} = 20$  k $\Omega$ .

Here we discuss how the effective resistances are achieved. When the topological switch is turned on, the resistance  $R_{jk}$  of the op-amp LT1063 in the unit cell is chosen as  $R_{12} = 1$  k $\Omega$ ,  $R_{13} = +\infty$  (which is realized by the open circuit),  $R_{14} = 10$  k $\Omega$ ,  $R_{17} = 2$  k $\Omega$ , and  $R_{28} = 2$  k $\Omega$ . Along the  $y$  direction, the op-amp is used to connect different unit cells. The resistance  $R_{jk}$  of the op-amp LT1063 is chosen as  $R_{17} = 2$  k $\Omega$ , and  $R_{28} = 2$  k $\Omega$ . Along the  $x$  direction, the op-amp is used to connect different unit cells. The resistance  $R_{jk}$  of the op-amp LT1063 is chosen as  $R_{13} = 1$  k $\Omega$ ,  $R_{14} = 10$  k $\Omega$ , and  $R_{23} = 10$  k $\Omega$ . For comparison, when the topological switch is turned off, the resistance  $R_{jk}$  of the op-amp LT1063 in the unit cell is chosen as  $R_{12} = 1$  k $\Omega$ ,  $R_{13} = +\infty$  (which is realized by the open circuit),  $R_{14} = 2$  k $\Omega$ ,  $R_{17} = 10$  k $\Omega$ , and  $R_{28} = 1$  k $\Omega$ . Along the  $y$  direction, the op-amp is used to connect different unit cells. The resistance  $R_{jk}$  of the op-amp LT1063 is chosen as  $R_{17} = 2$  k $\Omega$  and  $R_{28} = 6.2$  k $\Omega$ . Along the  $x$  direction, the op-amp is used to connect different unit cells. The resistance  $R_{jk}$  of the op-amp LT1063 is chosen as  $R_{13} = 6.2$  k $\Omega$ ,  $R_{14} = 10$  k $\Omega$ , and  $R_{23} = 10$  k $\Omega$ .

The slew rate of the op-amp LT1013 is 0.4V / $\mu$ s, while the time unit is milliseconds (ms) and the voltage unit is volts in the experiment. Therefore, the op-amp in our circuit works in the steady condition. The time error of relay G6K-2F-Y is about 0.1 ms. Errors between different relays may cause measurement errors.

The op-amp in the circuit can offset the losses caused by the resistance in the circuit. If the loss resistance  $g$  has value 0, the circuit matrix  $iA$  is a Hermitian matrix, and the loss caused by the resistance in the circuit just offsets the gains generated by the op-amp. Therefore, the square of the voltages does not decay and remain constant. This means that our structure can be extended arbitrarily, because the circuit losses are in balance with the op-amp gains.

However, due to the existence of internal resistance in the circuit, the electrical signals in the experiment still decay, but when the nonreciprocal transport disappears, the rate of pumping decay from left to right is the same as that pumping decay from right to left. We assume that this kind of circuit decay is completely attributed to the internal resistance in the circuit, and omit the decay by the internal resistance. This only results in a proportional change in the ordinate of the experimental results, and does not affect the results. Similarly, the balance between resistance losses and op-amp gains depends on the ratio of the resistance value in the op-amp structure. When there is resistance error or internal resistance in the circuit, the op-amp gains may be larger than resistance losses. As a result, the total square of the voltages may be greater than 1 at the beginning, as in our experiments (Fig. 4 in the main text).

- [1] C. M. Bender, Making sense of non-Hermitian hamiltonians, *Rep. Prog. Phys.* **70**, 947 (2007).
- [2] N. Moiseyev, *Non-Hermitian Quantum Mechanics* (Cambridge University Press, Cambridge, UK, 2011).
- [3] R. El-Ganainy, K. G. Makris, M. Khajavikhan, Z. H. Musslimani, S. Rotter, and D. N. Christodoulides, Non-Hermitian physics and  $\mathcal{PT}$  symmetry, *Nat. Phys.* **14**, 11 (2018).

- [4] M.-A. Miri and A. Alù, Exceptional points in optics and photonics, *Science* **363**, eaar7709 (2019).
- [5] D. Leykam, K. Y. Bliokh, C. Huang, Y. D. Chong, and F. Nori, Edge Modes, Degeneracies, and Topological Numbers in Non-Hermitian Systems, *Phys. Rev. Lett.* **118**, 040401 (2017).
- [6] L. Xiao, X. Zhan, Z. H. Bian, K. K. Wang, X. Zhang, X. P. Wang, J. Li, K. Mochizuki, D. Kim, N. Kawakami, W. Yi,

- H. Obuse, B. C. Sanders, and P. Xue, Observation of topological edge states in parity-time-symmetric quantum walks, *Nat. Phys.* **13**, 1117 (2017).
- [7] Z. Gong, Y. Ashida, K. Kawabata, K. Takasan, S. Higashikawa, and M. Ueda, Topological Phases of Non-Hermitian Systems, *Phys. Rev. X* **8**, 031079 (2018).
- [8] S. Yao and Z. Wang, Edge States and Topological Invariants of Non-Hermitian Systems, *Phys. Rev. Lett.* **121**, 086803 (2018).
- [9] F. K. Kunst, E. Edvardsson, J. C. Budich, and E. J. Bergholtz, Biorthogonal Bulk-Boundary Correspondence in Non-Hermitian Systems, *Phys. Rev. Lett.* **121**, 026808 (2018).
- [10] S. Yao, F. Song, and Z. Wang, Non-Hermitian Chern Bands, *Phys. Rev. Lett.* **121**, 136802 (2018).
- [11] E. Cobanera, A. Alase, G. Ortiz, and L. Viola, Generalization of Bloch's theorem for arbitrary boundary conditions: Interfaces and topological surface band structure, *Phys. Rev. B* **98**, 245423 (2018).
- [12] K. Kawabata, K. Shiozaki, and M. Ueda, Anomalous helical edge states in a non-Hermitian Chern insulator, *Phys. Rev. B* **98**, 165148 (2018).
- [13] C. Yin, H. Jiang, L. Li, R. Lü, and S. Chen, Geometrical meaning of winding number and its characterization of topological phases in one-dimensional chiral non-Hermitian systems, *Phys. Rev. A* **97**, 052115 (2018).
- [14] H. Jiang, C. Yang, and S. Chen, Topological invariants and phase diagrams for one-dimensional two-band non-Hermitian systems without chiral symmetry, *Phys. Rev. A* **98**, 052116 (2018).
- [15] T. Liu, Y. R. Zhang, Q. Ai, Z. Gong, K. Kawabata, M. Ueda, and F. Nori, Second-Order Topological Phases in Non-Hermitian Systems, *Phys. Rev. Lett.* **122**, 076801 (2019).
- [16] L. Jin and Z. Song, Bulk-boundary correspondence in a non-Hermitian system in one dimension with chiral inversion symmetry, *Phys. Rev. B* **99**, 081103(R) (2019).
- [17] T. E. Lee, Anomalous Edge State in a Non-Hermitian Lattice, *Phys. Rev. Lett.* **116**, 133903 (2016).
- [18] V. M. Martínez Alvarez, J. E. Barrios Vargas, and L. E. F. Foa Torres, Non-Hermitian robust edge states in one dimension: Anomalous localization and eigenspace condensation at exceptional points, *Phys. Rev. B* **97**, 121401(R) (2018).
- [19] B. Wang, T. Chen, and X. Zhang, Observation of novel robust edge states in dissipative non-hermitian quantum walks, *Laser Photonics Rev.* **14**, 2000092 (2020).
- [20] K. G. Makris, R. El-Ganainy, D. N. Christodoulides, and Z. H. Musslimani, Beam Dynamics in  $\mathcal{PT}$  Symmetric Optical Lattices, *Phys. Rev. Lett.* **100**, 103904 (2008).
- [21] A. Guo, G. J. Salamo, D. Duchesne, R. Morandotti, M. Volatier-Ravat, V. Aimez, G. A. Siviloglou, and D. N. Christodoulides, Observation of  $\mathcal{PT}$ -Symmetry Breaking in Complex Optical Potentials, *Phys. Rev. Lett.* **103**, 093902 (2009).
- [22] Y. Chong, L. Ge, and A. D. Stone,  $\mathcal{PT}$ -Symmetry Breaking and Laser-Absorber Modes in Optical Scattering Systems, *Phys. Rev. Lett.* **106**, 093902 (2011).
- [23] Z. Lin, H. Ramezani, T. Eichelkraut, T. Kottos, H. Cao, and D. N. Christodoulides, Unidirectional Invisibility Induced by  $\mathcal{PT}$ -Symmetric Periodic Structures, *Phys. Rev. Lett.* **106**, 213901 (2011).
- [24] A. Regensburger, C. Bersch, M. A. Miri, G. Onishchukov, D. N. Christodoulides, and U. Peschel, Parity-time synthetic photonic lattices, *Nature (London)* **488**, 167 (2012).
- [25] L. Feng, Y. Xu, W. S. Fegadolli, M. Lu, J. E. B. Oliveira, V. R. Almeida, Y. Chen, and A. Scherer, Experimental demonstration of a unidirectional reflectionless parity-time metamaterial at optical frequencies, *Nat. Mater.* **12**, 108 (2013).
- [26] J. W. Yoon, Y. Choi, C. Hahn, G. Kim, S. H. Song, K. Yang, J. Y. Lee, Y. Kim, C. S. Lee, J. K. Shin, H. Lee, and P. Berini, Time-asymmetric loop around an exceptional point over the full optical communications band, *Nature (London)* **562**, 86 (2018).
- [27] W. Chen, S. K. Özdemir, G. Zhao, J. Wiersig, and L. Yang, Exceptional points enhance sensing in an optical microcavity, *Nature (London)* **548**, 192 (2017).
- [28] H. Hodaie, A. U. Hassan, S. Wittek, H. Garcia-Gracia, R. El-Ganainy, D. N. Christodoulides, and M. Khajavikhan, Enhanced sensitivity at higher-order exceptional points, *Nature (London)* **548**, 187 (2017).
- [29] H. K. Lau and A. A. Clerk, Fundamental limits and non-reciprocal approaches in non-Hermitian quantum sensing, *Nat. Commun.* **9**, 4320 (2018).
- [30] S. Wang, B. Hou, W. Lu, Y. Chen, Z. Q. Zhang, and C. T. Chan, Arbitrary order exceptional point induced by photonic spin-orbit interaction in coupled resonators, *Nat. Commun.* **10**, 832 (2019).
- [31] Z. Y. Ge, Y. R. Zhang, T. Liu, S. W. Li, H. Fan, and F. Nori, Topological band theory for non-Hermitian systems from the Dirac equation, *Phys. Rev. B* **100**, 054105 (2019).
- [32] H. Xue, Q. Wang, B. Zhang, and Y. D. Chong, Non-Hermitian Dirac Cones, *Phys. Rev. Lett.* **124**, 236403 (2020).
- [33] A. Y. Song, X. Sun, A. Dutt, M. Minkov, C. Wojcik, H. Wang, I. A. D. Williamson, M. Orenstein, and S. Fan,  $\mathcal{PT}$ -Symmetric Topological Edge-Gain Effect, *Phys. Rev. Lett.* **125**, 033603 (2020).
- [34] H. Jiang and C. H. Lee, Dimensional transmutation from non-Hermiticity, [arXiv:2207.08843](https://arxiv.org/abs/2207.08843).
- [35] C. H. Lee, Exceptional Bound States and Negative Entanglement Entropy, *Phys. Rev. Lett.* **128**, 010402(2022).
- [36] C. H. Lee and R. Thomale, Anatomy of skin modes and topology in non-Hermitian systems, *Phys. Rev. B* **99**, 201103(R) (2019).
- [37] H. Jiang, L. J. Lang, C. Yang, S. L. Zhu, and S. Chen, Interplay of non-Hermitian skin effects and Anderson localization in nonreciprocal quasiperiodic lattices, *Phys. Rev. B* **100**, 054301 (2019).
- [38] N. Okuma, K. Kawabata, K. Shiozaki, and M. Sato, Topological Origin of Non-Hermitian Skin Effects, *Phys. Rev. Lett.* **124**, 086801 (2020).
- [39] K. Zhang, Z. Yang, and C. Fang, Correspondence between Winding Numbers and Skin Modes in Non-Hermitian Systems, *Phys. Rev. Lett.* **125**, 126402 (2020).
- [40] D. S. Borgnia, A. J. Kruchkov, and R.-J. Slager, Non-Hermitian Boundary Modes and Topology, *Phys. Rev. Lett.* **124**, 056802 (2020).
- [41] T. Helbig, T. Hofmann, S. Imhof, M. Abdelghany, T. Kiessling, L. W. Molenkamp, C. H. Lee, A. Szameit, M. Greiter, and R. Thomale, Generalized bulk-boundary correspondence in non-Hermitian topoelectrical circuits, *Nat. Phys.* **16**, 747 (2020).
- [42] L. Xiao, T. Deng, K. Wang, G. Zhu, Z. Wang, W. Yi, and P. Xue, Non-Hermitian bulk-boundary correspondence in quantum dynamics, *Nat. Phys.* **16**, 761 (2020).
- [43] A. Ghatak, M. Brandenbourger, J. van Wezel, and C. Coulais, Observation of non-Hermitian topology and its bulk-edge

- correspondence in an active mechanical metamaterial, *Proc. Natl. Acad. Sci. USA* **117**, 29561 (2020).
- [44] L. Li, C. H. Lee, and J. Gong, Impurity induced scale-free localization, *Commun. Phys.* **4**, 42 (2021).
- [45] W. Y. Deng, T. Chen, and X. D. Zhang,  $N$ th power root topological phases in Hermitian and non-Hermitian systems, *Phys. Rev. Res.* **4**, 033109 (2022).
- [46] W. Zhang, F. Di, H. Yuan, H. Wang, X. Zheng, L. He Xingen, H. Sun, and X. Zhang, Observation of non-Hermitian aggregation effects induced by strong interactions, *Phys. Rev. B* **105**, 195131 (2022).
- [47] L. Li and C. H. Lee, Non-Hermitian pseudo-gaps, *Sci. Bull.* **67**, 685 (2022).
- [48] T. Tai and C. H. Lee, Zoology of non-Hermitian spectra and their graph topology, [arXiv:2202.03462](https://arxiv.org/abs/2202.03462).
- [49] R. Yang, J. W. Tan, T. Tai, J. M. Koh, L. Li, S. Longhi, and C. H. Lee, Designing non-Hermitian real spectra through electrostatics, *Science Bulletin* **67**, 1865 (2022).
- [50] R. Shen and C. H. Lee, Non-Hermitian skin clusters from strong interactions, *Commun. Phys.* **5**, 238 (2022).
- [51] C. H. Lee, L. Li, and J. Gong, Hybrid Higher-Order Skin-Topological Modes in Nonreciprocal Systems, *Phys. Rev. Lett.* **123**, 016805 (2019).
- [52] D. Zou, T. Chen, W. He, J. Bao, C. H. Lee, H. Sun, and X. Zhang, Observation of hybrid higher-order skin-topological effect in non-Hermitian topoelectrical circuits, *Nat. Commun.* **12**, 7201 (2021).
- [53] L. S. Palacios, S. Tchoumakov, M. Guix, I. Pagonabarraga, S. Sánchez, and A. G. Grushin, Guided accumulation of active particles by topological design of a second-order skin effect, *Nat. Commun.* **12**, 4691 (2021).
- [54] L. Li, C. H. Lee, and J. Gong, Topological Switch for Non-Hermitian Skin Effect in Cold-Atom Systems with Loss, *Phys. Rev. Lett.* **124**, 250402 (2020).
- [55] M. Ezawa, Non-Hermitian boundary and interface states in nonreciprocal higher-order topological metals and electrical circuits, *Phys. Rev. B* **99**, 121411(R) (2019).
- [56] M. Ezawa, Non-Hermitian higher-order topological states in nonreciprocal and reciprocal systems with their electric-circuit realization, *Phys. Rev. B* **99**, 201411(R) (2019).
- [57] M. Ezawa, Braiding of Majorana-like corner states in electric circuits and its non-Hermitian generalization, *Phys. Rev. B* **100**, 045407 (2019).
- [58] C. H. Lee, S. Imhof, C. Berger, F. Bayer, J. Brehm, L. W. Molenkamp, T. Kiessling, and R. Thomale, Topoelectrical circuits, *Commun. Phys.* **1**, 39 (2018).
- [59] T. Hofmann, T. Helbig, C. H. Lee, M. Greiter, and R. Thomale, Chiral Voltage Propagation and Calibration in a Topoelectrical Chern Circuit, *Phys. Rev. Lett.* **122**, 247702 (2019).
- [60] S. Imhof, C. Berger, F. Bayer, J. Brehm, L. W. Molenkamp, T. Kiessling, F. Schindler, C. H. Lee, M. Greiter, T. Neupert, and R. Thomale, Topoelectrical-circuit realization of topological corner modes, *Nat. Phys.* **14**, 925 (2018).
- [61] A. Stegmaier, S. Imhof, T. Helbig, T. Hofmann, C. H. Lee, M. Kremer, A. Fritzsche, T. Feichtner, S. Klemmt, S. Höfling, I. Boettcher, I. C. Fulga, and L. Ma, Topological Defect Engineering and  $\mathcal{PT}$  Symmetry in Non-Hermitian Electrical Circuits, *Phys. Rev. Lett.* **126**, 215302 (2021).
- [62] S. Liu, S. Ma, C. Yang, L. Zhang, W. Gao, Y. J. Xiang, T. J. Cui, and S. Zhang, Gain- and Loss-Induced Topological Insulating Phase in a Non-Hermitian Electrical Circuit, *Phys. Rev. Appl.* **13**, 014047 (2020).
- [63] N. Q. Pan, T. Chen, H. J. Sun, and X. D. Zhang, Electric-circuit realization of fast quantum search, *Research (Wash., DC)* **2021**, 9793071 (2021).
- [64] H. X. Zhang, T. Chen, N. Q. Pan, and X. D. Zhang, Electric-circuit simulation of quantum fast hitting with exponential speedup, *Adv. Quantum Technol.* **5**, 2100143 (2022).
- [65] P. M. Lenggenhager, A. Stegmaier, L. K. Upreti, T. Hofmann, T. Helbig, A. Vollhardt, M. Greiter, C. H. Lee, S. Imhof, H. Brand, T. Kießling, I. Boettcher, T. Neupert, R. Thomale, and T. Bzdušek, Simulating hyperbolic space on a circuit board, *Nat. Commun.* **13**, 4373 (2022).
- [66] H. Hohmann, T. Hofmann, T. Helbig, S. Imhof, H. Brand, L. K. Upreti, A. Stegmaier, A. Fritzsche, T. Müller, U. Schwingenschlögl, C. H. Lee, M. Greiter, L. W. Molenkamp, T. Kießling, and R. Thomale, Observation of cnoidal wave localization in non-linear topoelectrical circuits, [arXiv:2206.09931](https://arxiv.org/abs/2206.09931).